









Cite this: DOI: 10.1039/d5ta04499e

# Liquid–liquid interfacial approach for the facile synthesis of Tp–NBD COFs for efficient photocatalytic hydrogen production

Syeda Andleeb Zahra Naqvi, <sup>ab</sup> Ateeq Ur Rehman Baloch, <sup>ab</sup> Umm Y. Umna, <sup>ab</sup> Kamran Muzaffar, <sup>ab</sup> Tayyab Sohail Aslam, <sup>ab</sup> Jinsong Chen<sup>\*abc</sup> and Yaobing Wang <sup>\*abc</sup>

The preparation of highly crystalline covalent organic frameworks (COFs) is crucial for the photocatalytic hydrogen ( $H_2$ ) evolution reaction (HER). However, it remains challenging because of the complicated structure of the monomer and the weakened interlayer interaction due to the large voids in the framework. Herein, a liquid–liquid interfacial (LLI) synthesis method was adopted for the spontaneous synthesis of Tp–NBD COFs at room temperature. The highly crystalline Tp–NBD COFs prepared under optimized conditions not only showed a uniformly distributed pore size of 0.6 nm and a BET specific surface area of  $677.5\text{ m}^2\text{ g}^{-1}$  but also exhibited enhanced the light absorption and promoted the charge separation. All these contributed to the photocatalytic HER activity of  $21\text{ mmol g}^{-1}\text{ h}^{-1}$  under AM 1.5 G irradiation, which was 24.4 times higher than that exhibited by the COF prepared by traditional solvothermal method, and it was remarkable among the pristine Tp COFs. The LLI method is expected to be extended for preparing COFs with functional groups for further enhancements in photocatalytic activities.

Received 4th June 2025

Accepted 27th July 2025

DOI: 10.1039/d5ta04499e

rsc.li/materials-a

## Introduction

Photocatalytic hydrogen ( $H_2$ ) evolution reaction (HER) from  $H_2O$ <sup>1,2</sup> is generally considered a promising solution<sup>3–8</sup> in the face of energy crisis and environmental hazards resulting from the overuse of fossil fuels.<sup>9–11</sup> However, the efficiency of the long-established semiconductor HER photocatalysts, such as  $TiO_2$ ,<sup>12</sup>  $CdS$ ,<sup>13</sup>  $g\text{-}C_3N_4$ ,<sup>14</sup> and metal organic frameworks (MOFs),<sup>15</sup> remains unsatisfactory as a result of the following reasons: (1) the insufficient absorption of visible light irradiation, which is the major part of solar irradiation;<sup>16</sup> (2) the sluggish mass transfer of the reactants;<sup>17</sup> (3) the easy recombination of photogenerated carriers;<sup>18</sup> and (4) the photo-corrosion of some materials.<sup>19</sup> Thus, exploring new and efficient photocatalysts with tunable characteristics for the photocatalytic HER activities is essential.<sup>20</sup>

Since their discovery in 2005,<sup>21</sup> covalent organic frameworks (COFs) have evolved as porous, crystalline materials assembled

with organic molecules *via* covalent bonds, possessing delocalized planar  $\pi\text{-}\pi$  stacking and ordered porous networks.<sup>22–24</sup> COFs have gained significant attention for their applications in the photocatalytic HER as they address the above shortcomings. The  $\pi\text{-}\pi$  conjugation in their network leads to a red-shifted absorption, thereby resulting in a more effective utilization of solar irradiation.<sup>25,26</sup> The intrinsic porosity of COFs facilitates the mass transfer of the reactants, leading to an improved catalytic performance. Moreover, COFs are constructed by integrating organic building blocks, which enables the design of photocatalysts with donor–acceptor (D–A) properties, facilitating efficient charge separation. Besides, the covalent bonds in the frameworks enhance their stability in the photocatalytic HER processes.<sup>27–30</sup>

Among several linkages,  $\beta$ -ketoenamine-linked COFs (Tp–COFs) are notable due to their high structural stability, high density of active sites, strong light-harvesting abilities, and reduced charge recombination.<sup>31</sup> In particular, the Tp–NBD COFs (Tp: (1,3,5-triformylphloroglucinol) and NBD: ( $N_4,N_4$ -bis(4'-amino-[1,1'-biphenyl]-4-yl)-[1,1'-biphenyl]-4,4'-diamine) monomers) is attractive as the  $C_3$  NBD monomer contains an electron-rich N atom and the biphenyl rings may create large pores in the constructed COFs. All these characteristics contribute to enhancing the photocatalytic HER activities. However, the synthesis of this COF is challenging due to its reduced growth rate, as a result of the weakened van der Waals interaction at the interface, which stems from the N atom with

<sup>a</sup>CAS Key Laboratory of Design and Assembly of Functional Nanostructures, Fujian Provincial Key Laboratory of Nanomaterials, State Key Laboratory of Structural Chemistry, Fujian Institute of Research on the Structure of Matter, Chinese Academy of Sciences, Fuzhou 350002, Fujian, P. R. China. E-mail: chenjs@fjirsm.ac.cn; wangyb@fjirsm.ac.cn

<sup>b</sup>University of Chinese Academy of Sciences, Beijing 100049, P. R. China

<sup>c</sup>Fujian Science and Technology Innovation Laboratory for Optoelectronic Information of China, Fuzhou 350108, Fujian, P. R. China



lone pair electrons reducing the planarity of the NBD monomer and the biphenyl rings, increasing the ratio of the void in the unit cell of the COFs. The  $\beta$ -ketoenamine linkage is formed through structural reconstruction *via* combined reversible and irreversible routes<sup>32</sup> through bond shifting, keeping the atomic positions unchanged.<sup>33</sup> Despite their stable structures,<sup>34</sup> the enhanced crystallinity and increased porosity are crucial for promoting the photocatalytic HER activities of Tp-COFs. Numerous studies have been conducted on improving crystallinity of Tp-COFs while maintaining their stability, as their frameworks are susceptible to bond breakage, stacking breakdown or flexible pore collapse under harsh synthesis conditions.<sup>35</sup> Conventional solvothermal methods used to synthesize Tp-COFs do not allow such optimizations due to the high-energy input over an extended period, complex procedures, and possible loss of crystallinity. Therefore, a suitable synthesis method is required that allows control over reaction parameters influencing the structural properties of COFs.

Recently, a new synthetic strategy, named liquid-liquid interfacial (LLI), was introduced for the rapid synthesis of COFs under ambient conditions.<sup>36</sup> In the LLI synthesis method, the aldehyde and amine monomers are dispersed separately in miscible organic solvents, which allows the monomers to rearrange themselves into planar oligomers prior to COF formation.<sup>37</sup> A low-density solvent (acetic acid (HoAc)) is used as a buffer interlayer to prevent the intermixing of the two miscible organic solvents, which effectively controls the rate of diffusion and interaction of oligomers,<sup>38</sup> thus maintaining crystallinity, resulting in a finely tuned morphology, surface area and pore size. This synthetic method has been widely adopted in the synthesis of highly porous COFs, such as Tp-BD(OH)<sub>2</sub> COF,<sup>39</sup> (TpAzo, TpDPP, TpOMeAzo, TpOMeDPP) COFs,<sup>40</sup> and FS-COM-1/2 COFs.<sup>38</sup> All these COFs show notable performance in related applications. Since this method promises high crystallinity, we employed it to fabricate a series of pristine Tp-COFs. Although the LLI method has been widely used to synthesize COF films and membranes, it has not been reported for the synthesis of COFs for the photocatalytic HER activities to the best of our knowledge. Since the LLI method works well for the synthesis of self-standing FS-COM-1/2 COFs containing the non-planar TAPA monomer,<sup>38</sup> it is reasonable to expect that the LLI can be extended for the synthesis of Tp-NBD COFs composed of the non-planar NBD monomer.

Herein, we report a scalable and spontaneous interfacial synthesis of highly crystalline Tp-NBD COFs at ambient conditions, without requiring post-synthetic modification, exfoliation, or composite formation. Based on the results of various characterizations and theoretical calculations, it is discovered that the crystallinity and porosity of the prepared samples can be controlled by adjusting the concentration of the catalyst (acetic acid (HoAc)) at the interface. HoAc restricts polymerization at the interface between the two immiscible organic phases, which leads to an ordered framework with high crystallinity and increased surface area.<sup>41</sup> Moreover, compared with the Tp-NBD COFs prepared *via* the traditional solvothermal method (12 M/Tp-NBD (ST)), the optimal LLI Tp-NBD COFs prepared using 12 M HoAc shows enhanced

crystallinity, which brings about increased specific surface area and uniformly distributed pores, but more importantly, better absorption of radiation, proper energy band positions and promoted charge separation efficiency. Consequently, the 12 M/Tp-NBD (LLI) COF shows an HER activity of 21 mmol g<sup>-1</sup> h<sup>-1</sup>, 24.4 times higher than that of the 12 M/Tp-NBD (ST) COF. Moreover, the activity is also high among pristine Tp COFs. This extends the utility of the LLI method beyond membranes, providing a scalable route to COF-based photoactive systems with heteroatoms or functionalized groups, further promoting the photocatalytic HER activities.

## Results and discussion

### Synthesis and characterization

The  $\beta$ -ketoenamine Tp-NBD COFs were designed and synthesized using the liquid-liquid interface (LLI) method at room temperature (Fig. 1a and Scheme S1). The COFs with  $\beta$ -ketoenamine linkages were successfully synthesized instantly *via* the Schiff-base condensation reaction between Tp (1,3,5-triformylphloroglucinol) and NBD (*N,N*-bis(4'-amino-[1,1'-biphenyl]-4-yl)-[1,1'-biphenyl]-4,4'-diamine), using different molar concentrations of acetic acid, based on which the COFs were named 3 M/Tp-NBD, 6 M/Tp-NBD, 9 M/Tp-NBD, 12 M/Tp-NBD, 15 M/Tp-NBD and 17 M/Tp-NBD. Moreover, a solvothermal analogue (12 M/Tp-NBD (ST)) with 12 M HoAc was synthesized *via* a conventional method (Scheme S2) to rationally investigate the effect of the synthetic method on morphology,<sup>38</sup> crystallinity and photoactivity of the as-synthesized COFs. One of the distinctive features of interfacial condensation for preparing Tp-COFs is that the monomers undergo a fast fusion to produce oligomers, which then self-assemble slowly at the interface with regular crystalline networks. The 12 M/Tp-NBD COF exhibited higher crystallinity, porosity, and photoactivity among the as-synthesized four samples. The crystallinity of the related COFs was analyzed using powder X-ray diffraction (PXRD) and structural simulations using Materials Studio. The simulated XRD patterns obtained *via* Pawley refinement and the AA-stacking model aligned well with the experimental results (Fig. 1b and c). The as-synthesized COFs exhibited a highly ordered honeycomb lattice, with the corresponding lattice parameters being  $a = b = 25.586$  Å,  $c = 3.542$  Å, and  $\alpha = \beta = 90^\circ$ ,  $\gamma = 120^\circ$  in the *P1* space group. The refined PXRD patterns of the 12 M/Tp-NBD COF obtained by Pawley Refinement were consistent with the experimental data ( $R_p = 3.15\%$ ,  $R_{wp} = 4.05\%$ ). The sharp peak at  $2\theta \sim 4.15^\circ$  is attributed to the strong reflection from the (100) facet, while the broad peak around  $2\theta \sim 20^\circ$  corresponds to the (001) facet arising from the interlayer stacking in the COF network. The high-intensity peak (100) demonstrates the high crystallinity of the as-synthesized LLI COFs reported in this study. The FWHM analysis of the (100) diffraction peak for LLI COFs also indicates that the crystallinity increases with increasing HoAc concentration at the interface. 12 M/Tp-NBD exhibited the lowest FWHM of  $0.29^\circ$ , suggesting a more ordered framework and enhanced crystallinity among nM/Tp-NBD COFs. The PXRD peaks of 3–17 M/Tp-NBD, 12 M/Tp-NBD (ST) and their comparison with 12 M/Tp-NBD, along



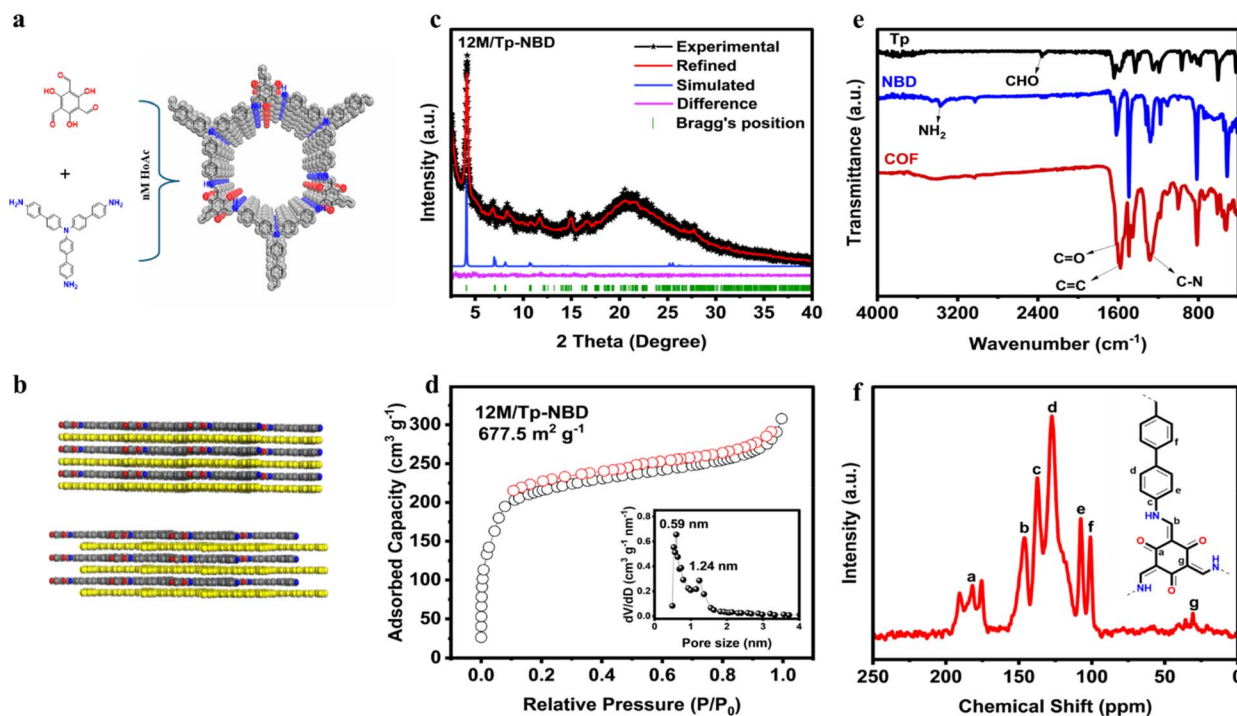


Fig. 1 (a) Liquid–liquid interfacial (LLI) synthesis of Tp–NBD COFs, (b) with AA and AB stacking models. (c) PXRD peaks of experimental and simulated patterns. (d)  $N_2$  adsorption–desorption isotherm (77 K) (inset: pore size distribution by NLDFT method), (e) FT-IR spectra, and (f)  $^{13}C$  solid-state NMR spectrum of 12 M/Tp–NBD COF, inset is the model compound.

with their FWHM values, are reported in the SI (Fig. S1–S7). It is evident from Fig. S6 that the 12 M/Tp–NBD (ST) COF has a poor crystallinity, with a much broader PXRD peak, as compared to the as-synthesized LLI COFs. Moreover, when compared with the PXRD patterns of 15 M/Tp–NBD COF and 17 M/Tp–NBD COF, it can be inferred that increasing the HoAc catalyst concentration to 12 M induces significant changes in the morphology, surface texture and the HER activities of the COFs, resulting in spherical structures, whereas further increases in HoAc concentration causes only subtle changes. Thus, the COF prepared under 12 M HoAc was subjected to more detailed characterizations and analysis.

The  $N_2$  adsorption–desorption isotherms calculated at 77 K exhibited type-I sorption isotherms and microporous characteristics for as-synthesized COFs, where 12 M/Tp–NBD exhibited the highest surface area of  $677.5 \text{ m}^2 \text{ g}^{-1}$  with a pore volume ( $P/P_0$ ) of  $0.47 \text{ cm}^3 \text{ g}^{-1}$ , with the pore size distribution between 0.60 nm and 1.24 nm based on the non-local density functional theory calculations (Fig. 1d). Interestingly, the surface area and pore volume of 12 M/Tp–NBD COF are greater than those of 3 M, 6 M and 9 M/Tp–NBD COFs, as well as 12 M/Tp–NBD (ST) COF, which suggests that despite the same chemical composition, different structural arrangements can control the pore shrinkage and adjust their specific surface area. Interface mediation enables precise control over interlayer stacking and planarity, resulting in a self-regulating network with high surface area.<sup>38</sup> The Brunauer–Emmett–Teller (BET) surface area of 3–17 M/Tp–NBD, 12 M/Tp–NBD (ST) COFs and their corresponding pore volumes are listed in the SI (Fig. S8–S14 and

Table S1). Notably, the surface area of the COF synthesized *via* the solvothermal method is low, with poor pore size distribution, which further confirms the superiority of the LLI method. The defined chemical structures and components of 12 M/Tp–NBD COF were investigated using Fourier transform infrared (FT-IR) spectroscopy,  $^{13}C$  cross-polarization/magic angle spinning solid-state nuclear magnetic resonance (CP/MAS-ssNMR) spectroscopy and X-ray photo spectroscopy (XPS). The successful formation of the  $\beta$ -ketoenamine linkage in 12 M/Tp–NBD was confirmed by the disappearance of the typical absorption peaks of  $-\text{NH}_2$  ( $\sim 3360 \text{ cm}^{-1}$ ) and  $-\text{CHO}$  ( $\sim 1640 \text{ cm}^{-1}$ ), and the emergence of the intense stretching peak of the  $-\text{C}=\text{C}$  bond around  $\sim 1590 \text{ cm}^{-1}$ . In contrast, a strong peak for  $=\text{C}-\text{N}$  appeared around  $\sim 1285 \text{ cm}^{-1}$ , confirming the presence of keto-form (Fig. 1e). The FT-IR spectra of 3–9 M/Tp–NBD and 12 M/Tp–NBD (ST) are presented in the SI (Fig. S15 and S16). The  $^{13}C$  CP/MAS-ssNMR spectrum of 12 M/Tp–NBD COF revealed resonance signals at  $\sim 182 \text{ ppm}$  and  $\sim 146 \text{ ppm}$ , corresponding to  $-\text{C}=\text{O}$  ( $\beta$ -keto group) and  $-\text{C}=\text{C}-\text{N}$  (enamine) bonds, respectively, revealing the keto-enamine tautomerism. Moreover, the absence of a  $\sim 160 \text{ ppm}$  signal for  $-\text{C}=\text{N}$  (enol form) further confirms the formation of a ketoenamine bond (Fig. 1f). This ketoenamine linkage is the defining feature of Tp–NBD COFs, which governs its stability, polarity, and light-harvesting ability.<sup>42</sup>

XPS spectra were recorded for 12 M/Tp–NBD COF to elucidate the structural compositions further (Fig. 2a, b and S17). In the C 1s signal, there are three different types of carbon atoms, ascribed to  $\text{C}=\text{C}$  or  $\text{C}-\text{C}$  ( $\sim 284.9 \text{ eV}$ ),  $\text{C}-\text{N}$  ( $\sim 286.0 \text{ eV}$ ), and





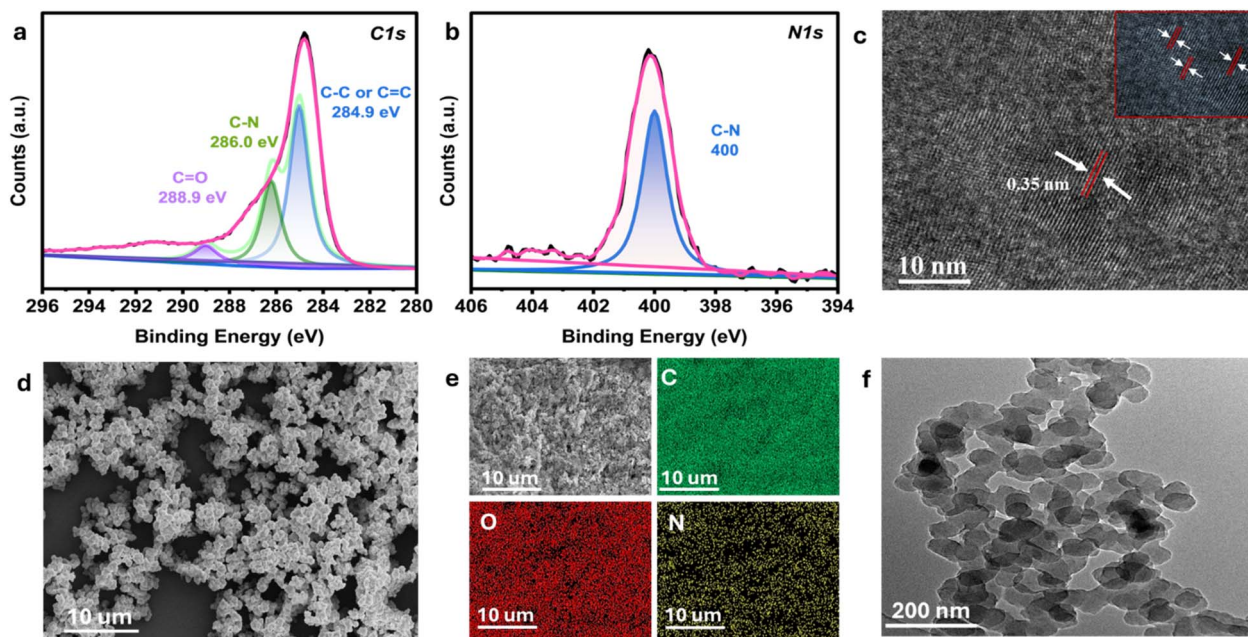


Fig. 2 (a and b) High-resolution XPS scans of C 1s and N 1s spectra. (c) High-resolution TEM image; (d) SEM image; (e) EDAX elemental mapping images for C, N, O; and (f) TEM image of 12 M/Tp-NBD COF.

C=O ( $\sim 288.9$  eV). The binding energy at  $\sim 400$  eV in the N 1s spectrum is ascribed to the N atoms of the C–N bond, indicating the successful formation of the  $\beta$ -ketoenamine bonds in 12 M/Tp-NBD COF.<sup>43</sup> The results of XPS spectra align well with those of  $^{13}\text{C}$  CP/MAS-ssNMR and FT-IR spectra, further confirming the successful synthesis of keto-COFs. The high-resolution transmission electron microscopy (HR-TEM) showed ordered lattice fringes with spatial layers arranged at 0.35 nm, observed for the interlayer stacking, which is in close agreement with the (001) diffraction peak at  $2\theta \approx 20^\circ$ , indicating periodic stacking, commonly stabilized by  $\pi$ - $\pi$  interactions (Fig. 2c). The morphologies of 3–17 M/Tp-NBD COFs were evaluated using scanning electron microscopy (SEM), and uniform elemental distribution of carbon (C), nitrogen (N), and oxygen (O) was confirmed from energy dispersive X-ray analysis (EDAX) mapping (Fig. 2d and e). The morphologies of the four COFs were affected by the different concentrations of acetic acid, which changed from sheet-like (3–6 M/Tp-NBD) to nanoparticles (9–17 M/Tp-NBD) with increasing acetic acid concentrations as presented in SI (Fig. S20–S22). Transmission electron microscopy (TEM) images provided the high-resolution internal structural and crystallographic details of Tp-NBD COFs, further confirming their morphology (Fig. 2f and S23–S28). Additionally, all nM/Tp-NBD COFs exhibited excellent thermal stability up to 593  $^\circ\text{C}$  (Fig. S29).

### Opto-electronic properties

Solid-state ultraviolet-visible diffuse reflectance spectra (UV-vis DRS) displayed that 3–12/Tp-NBD COFs had strong light-absorption efficiency with absorption edges higher than 650 nm, covering ultraviolet to visible light regions (Fig. 3a). The

optical band gap ( $E_g$ ) of 12 M/Tp-NBD COF measured through Tauc plot transformation from UV-vis DRS was 1.83 eV (Fig. 3a and S30), consistent with the theoretical findings. However, 12 M/Tp-NBD (ST) COF exhibits poor light-harvesting ability, indicating that the harsh synthesis conditions affect the crystallinity, surface characteristics, and optical properties of the COF. The band gap for the 12 M/Tp-NBD (ST) COF is also 1.83 eV, but shows a much lower absorption to the irradiation. This results from its lower crystallinity and reduced conjugation

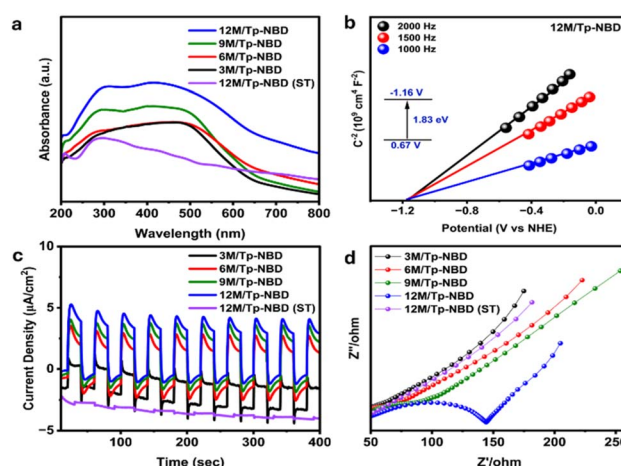


Fig. 3 Optoelectronic properties: (a) UV-vis DRS spectra of 3–12 M/Tp-NBD and 12 M/Tp-NBD (ST) COFs. (b) Mott–Schottky curve for 12 M/Tp-NBD COF. (c) transient on/off photocurrent responses under visible light irradiation ( $\lambda \geq 420$  nm, 300 W Xe lamp), and (d) Nyquist plots of EIS measurements of 3–12 M/Tp-NBD and 12 M/Tp-NBD (ST).



effect within the framework. Mott–Schottky (MS) measurements were performed to elucidate the band positions of all Tp–NBD COFs (Table S2). The positive slopes indicated that all COFs were typical n-type semiconductors (Fig. S31). The flat-band potential recorded from MS measurements for 12 M/Tp–NBD COFs was  $-1.16$  V vs. NHE (Fig. 3b). However, it is interesting to see that the CB potential for the 12 M/Tp–NBD (ST) is  $-0.46$  V, and the VB potential is  $1.37$  V. Compared with the 12 M/Tp–NBD COF, the CB potential of the 12 M/Tp–NBD (ST) COF is not beneficial for the photocatalytic HER.

Accordingly, the corresponding band gaps of nM/Tp–NBD COFs were calculated, and all the CB reduction potentials lie above the potential of  $\text{H}^+/\text{H}_2$  ( $-0.41$  V at pH = 7), illustrating that protons can be reduced to hydrogen under thermodynamically preferred conditions.<sup>23</sup> Thus, considering their broad absorption spectra and suitable energy levels, the prepared nM/Tp–NBD LLI COFs would have the potential for applications in photocatalytic hydrogen production (Fig. S32). Under visible light irradiation, the as-synthesized COF samples were evaluated for their photocurrent responses in a three-electrode cell using  $0.5$  M  $\text{Na}_2\text{SO}_4$  aqueous solution as an electrolyte<sup>44</sup> to evaluate the dynamics of photogenerated charge carriers in Tp–NBD COFs. The as-synthesized Tp–NBD COFs exhibited consistent and repeatable on–off cycles, demonstrating strong photoresponse and excellent structural stability when exposed to light (Fig. 3d). The 12 M/Tp–NBD COF exhibited the highest photocurrent density, remarkably exceeding 3 M, 6 M, and 9 M/Tp–NBD COFs. The enhanced photocurrent response indicates a more effective charge separation and transport of photogenerated electron–hole pairs, which can be linked to the enhanced interfacial conductivity and superior light-harvesting ability of 12 M/Tp–NBD COF. However, the photocurrent response of 12 M/Tp–NBD (ST) COF is very poor, which indicates a poor charge separation ability, leading to a very low photocatalytic HER activity. The photoresponse for all COFs was in the order of 12 M/Tp–NBD > 9 M/Tp–NBD > 6 M/Tp–NBD > 3 M/Tp–NBD > 12 M/Tp–NBD (ST) (Fig. 3c). These values aligned with the trend of their HER activities, confirming better photo-response ability and more available photogenerated carriers in 12 M/Tp–NBD COF. The electronic conductivity and facilitated charge transfer ability of these COFs were also confirmed by their EIS measurements, where 12 M/Tp–NBD exhibited the smallest radius in the Nyquist plot (Fig. 3d). The diameter of the semicircle observed in the high-resistance area represents the charge transfer resistance ( $R_{\text{ct}}$ ) at the interface. Among all samples, 12 M/Tp–NBD COF displayed the smallest semicircle, signifying the lowest  $R_{\text{ct}}$  and the most effective interfacial charge transfer. The observed trend in photocurrent intensity is in close agreement with the EIS results, which confirm that the control over the structure–property relationship significantly enhances charge mobility, reduces charge recombination, and improves overall photocatalytic performance.<sup>45</sup> The time-resolved photoluminescence (TR-PL) spectroscopy showed that the average decay lifetime of 12 M/Tp–NBD COF was  $0.937$  ns, the longest lifetime among the four COFs reported in this study (Fig. S33 and S34). The longer lifetime might be ascribed to its  $\pi$ -extended conjugation and the ordered D–A structures

that effectively promote charge transfer and separation. Thus, enhanced photo-response ability, more available photogenerated carriers, good electronic conductivity, and efficient charge separation are believed to be the reasons for the excellent hydrogen evolution performance for this COF, remarkably exceeding the most reported pristine Tp–COFs.

### Photocatalytic $\text{H}_2$ evolution activities

Different control experiments on 12 M/Tp–NBD COF were conducted to evaluate the optimal reaction system for enhanced photo-activity. Among the three sacrificial agents (ascorbic acid (AA), sodium ascorbate (SA), and triethanolamine (TEOA)) tested, AA works better than the other sacrificial agents for photo-activity due to its efficient hole-trapping ability. Firstly, the reaction system was subjected to photo-HER without AA. As expected, there was no hydrogen production, further confirming the important role of ascorbic acid in the reaction system. This can be explained by the lower oxidation potential of the hole ( $\text{h}^+$ ) in the HOMO of the COF. Notably, the reaction system exhibited hydrogen evolution even without Pt (Fig. S36). The effect of acetic acid (AA) concentration on the photocatalytic hydrogen evolution reaction (HER) performance of 12 M/Tp–NBD COF was systematically investigated, where the HER rate increased significantly with higher AA concentrations (Fig. S37). Negligible hydrogen evolution was observed when the system was kept in the dark (Fig. S38). To evaluate the photocatalytic HER activity, different amounts of pristine COF were dispersed in a  $100$  mL aqueous solution of  $0.05$  M AA as a sacrificial reagent and  $20$   $\mu\text{L}$  of  $0.01$  M  $\text{H}_2\text{PtCl}_6 \cdot 6\text{H}_2\text{O}$  as the source of Pt co-catalyst. Among the different amounts,  $3$  mg COF exhibited a stable photocatalytic activity over a longer reaction time

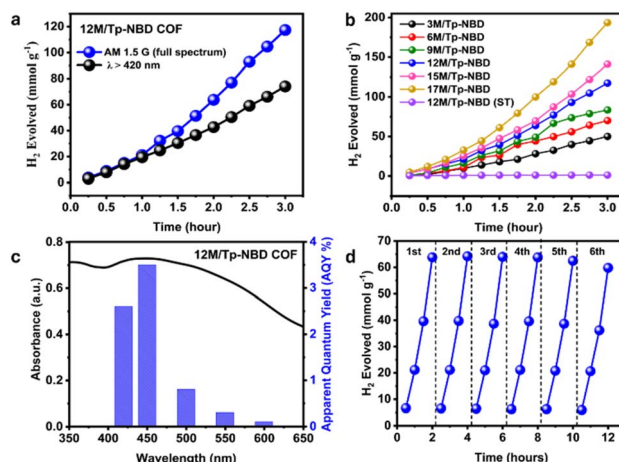


Fig. 4 (a) Photocatalytic HER activity curve of 12 M/Tp–NBD COF under irradiation (Xe lamp, 300 W); (blue curve) AM 1.5 G light source; (black curve)  $\lambda = 420$  nm, (b) rate of the photocatalytic HER using AM 1.5 G light source for 3–12 M/Tp–NBD and 12 M/Tp–NBD (ST) COFs (3 mg catalyst in  $100$  mL water, 2 wt% Pt ( $0.01$  M  $\text{H}_2\text{PtCl}_6$ ),  $0.05$  M ascorbic acid), (c) absorption spectrum and wavelength-specific AQY, and (d) photocatalytic cyclic stability test for 12 M/Tp–NBD COF (the reaction system was evacuated for 20 minutes after each cycle without the use of any additional AA or Pt).





(Fig. S39). Fig. 4a shows the rate of HER under full-spectrum irradiation (AM 1.5 G) and at wavelengths longer than 420 nm. The HER values were determined to be 21.1 and 19.3 mmol g<sup>-1</sup> h<sup>-1</sup>, respectively. Upon irradiation with an AM 1.5 G light source (xenon lamp 300 W), 12 M/Tp-NBD exhibited the highest HER activity of 21 mmol g<sup>-1</sup> h<sup>-1</sup>, as compared to 3 M/Tp-NBD (9.7 mmol g<sup>-1</sup> h<sup>-1</sup>), 6 M/Tp-NBD (10.6 mmol g<sup>-1</sup> h<sup>-1</sup>), 9 M/Tp-NBD (16 mmol g<sup>-1</sup> h<sup>-1</sup>) and 12 M/Tp-NBD (ST) (0.86 mmol g<sup>-1</sup> h<sup>-1</sup>) COFs (Fig. 4b). It should be noted that although the light-harvesting capabilities of the four LLI COFs are similar, there are significant differences in their photocatalytic HER activities. The photocatalytic HER activity of 12 M/Tp-NBD COF (21 mmol g<sup>-1</sup> h<sup>-1</sup>) is twice the rate of HER for 3 M/Tp-NBD COF (9.7 mmol g<sup>-1</sup> h<sup>-1</sup>), which might originate from the more ordered D-A structure of 12 M/Tp-NBD COF. The well-ordered D-A structure facilitates the efficient separation of photogenerated electrons and holes, thereby boosting the photo-activity.<sup>46</sup> Under the same reaction conditions, despite their similar chemical composition, the difference in photo-activity also arises due to the difference in their surface areas, which is much higher for 12 M/Tp-NBD (677.5 m<sup>2</sup> g<sup>-1</sup>) than for 3 M/Tp-NBD (63.4 m<sup>2</sup> g<sup>-1</sup>), 6 M/Tp-NBD (311.5 m<sup>2</sup> g<sup>-1</sup>), and 9 M/Tp-NBD (391.6 m<sup>2</sup> g<sup>-1</sup>). This indicates that precise control over surface area can directly influence the performance of the as-synthesized COFs.<sup>26,47</sup> Moreover, smaller orderly assembled nanoparticles, as in the case of 12 M/Tp-NBD COF, instead of irregular aggregates as in 12 M/Tp-NBD (ST) COF, lead to higher surface-to-volume ratios and more mismatched atoms on their surface, which can create a more defined crystalline domain to improve photocatalytic activity.<sup>48</sup> The separation efficiency of photogenerated electrons and holes evaluated through the photocurrent and EIS measurements further explains the differences in photocatalytic activities of these COFs. The initially formed imine linkage undergoes irreversible tautomerization to form  $\beta$ -ketoenamine linkages, enhancing the framework's chemical stability and electron delocalization. The stable structure features extended conjugation and active sites, which facilitate efficient charge separation and proton reduction.<sup>23</sup> Therefore, the  $\beta$ -ketoenamine linkage in these Tp-NBD COFs stabilizes the COF structure and enhances its photocatalytic activity for HER (Fig. S40). 3–17 M/Tp-NBD COFs were further subjected to evaluate the apparent quantum yields (AQYs) under different monochromatic lights. It was found that 12 M/Tp-NBD COF has the highest AQY (3.5%) at 450 nm (Fig. 4c). The AQYs of 3–17 M/Tp-NBD COFs were also measured at various wavelengths (Fig. S41 and Table S3), which followed their trend of visible light absorption. Moreover, 12 M/Tp-NBD COF exhibited no substantial decrease in its photocatalytic hydrogen evolution rate after six cycles with continuous irradiation under visible light, confirming its long-term photocatalytic stability (Fig. 4d). The HER activities of these COFs remarkably exceeded the most reported pristine Tp-COFs (Table S4). After the photocatalytic HER tests, the recycled 12 M/Tp-NBD COF was subjected to systematic characterizations, including PXRD, FT-IR, XPS, SEM, TEM, and UV-vis DRS. The results of these characterizations remain almost unchanged compared with the ones before the reaction, further confirming

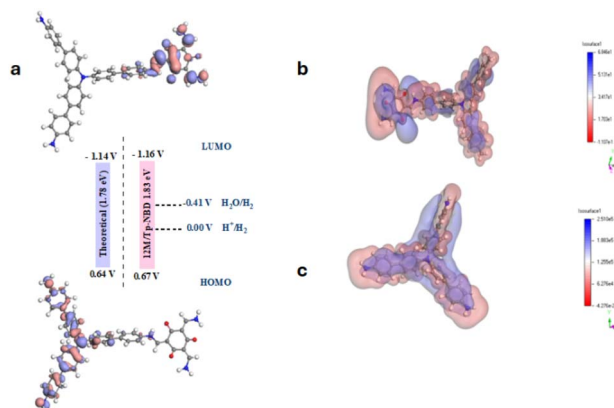


Fig. 5 (a) HOMO–LUMO surface plots and band gap diagram from theoretical (blue bar) and experimental (pink bar) calculations and (b and c) electrostatic potential of Tp–NBD COFs.

the structural stability of the COF synthesized *via* the liquid–liquid interfacial method (Fig. S42–S52).

DFT calculations were conducted to obtain further electronic structure information of Tp–NBD COFs, including the redox potential of the conduction band minimum (CBM) and valence band maximum (VBM). The CBM orbital electrons are mainly localized in the Tp cores in Tp–NBD COFs, while those of the VBM orbital are distributed along the NBD regions (Fig. 5a).<sup>49</sup> This suggests the Tp core is electron-deficient and could act as an efficient electron-acceptor moiety. In Tp–NBD COFs, the ketone unit in the Tp moiety acts as an electron-deficient center, while the aromatic diamine linkages in NBD serve as electron donors, imparting molecular polarity and facilitating charge stabilization and transfer to active sites for HER performance (Fig. 5b and c).<sup>31</sup> The uniformity of charge distribution in CBM and VBM of Tp–NBD COFs indicates higher photoconductivity. The above situation also exists in the theoretical calculations, where a band gap of 1.78 eV was calculated (Fig. 5c), further suggesting that Tp–NBD COFs is suitable for photocatalytic HER under visible light irradiation.<sup>50</sup> The experimental and theoretical findings of this study suggest that all nM/Tp–NBD COFs are suitable for absorbing visible light for photocatalytic hydrogen production.<sup>51</sup> Notably, control over the synthesis method enhances the surface area, degree of conjugation and electron delocalization. Therefore, a higher surface area leads to a higher conjugation degree and better photocatalytic activity,<sup>52</sup> which provides a new perspective for the development of photocatalysts.

## Conclusions

In summary, we designed and synthesized a series of  $\pi$ -conjugated Tp–NBD COFs *via* the liquid–liquid interfacial (LLI) method. The microscopic morphologies of the samples can be tuned by adding different concentrations of acetic acid at the interface. Compared with the Tp–NBD COFs prepared by the solvothermal method and other Tp–NBD COFs prepared by the LLI method, the optimized 12 M Tp–NBD COF shows



significantly enhanced crystallinity, which brings about a higher specific surface area. Moreover, the light absorption capacity was extended, and the separation of photogenerated charge carriers was promoted. Consequently, a remarkably enhanced and stable photocatalytic HER activity of up to 21 mmol g<sup>-1</sup> h<sup>-1</sup> was achieved under irradiation. This study demonstrates that pronounced surface properties are crucial for the extraction, accumulation, and transfer of photoinduced electrons. Therefore, our work presents a promising strategy for tuning the surface properties of COF, and it is expected that the LLI synthetic method can be extended to the synthesis of COF photocatalysts with more complicated structures for further enhanced activities.

## Author contributions

S. A. Z. Naqvi contributed to the investigation, data curation, conceptualization, methodology, formal analysis, and writing the original draft. A. U. R. Baloch, U. Y. Umna, K. Muzaffar and T. S. Aslam were responsible for investigation, curation and formal data analysis. J. Chen was responsible for the formal analysis, review & editing. Y. Wang was responsible for the conceptualization, project administration, supervision, funding acquisition, and resources.

## Conflicts of interest

The authors declare no conflict of interest.

## Data availability

The data supporting this article (experimental details, calculation methods and supplementary figures and tables) have been included as part of the SI. See DOI: <https://doi.org/10.1039/d5ta04499e>.

## Acknowledgements

This work is supported by the National Natural Science Foundation of China (grant no. 22425904, 22279141) (Y. W.), Key Research Program of Frontier Sciences, CAS (grand no. ZDBS-LY-SLH028) (Y. W.), National Key Research & Development Program of China (grant no. 2021YFA1501500) (Y. W.), and Fujian Science & Technology Innovation Laboratory for Optoelectronic Information of China (grant no. 2021ZZ106) (Y. W.) The author, S. A. Z. Naqvi, is also thankful for the CSC scholarship by the University of Chinese Academy of Sciences, China, supporting doctoral studies. We want to thank Dr Xiao-Liang Ye for his timely assistance and patient explanation of the TEM analysis.

## Notes and references

- 1 F. Wen and C. Li, *Acc. Chem. Res.*, 2013, **46**, 2355–2364.
- 2 J.-R. Shen, *Annu. Rev. Plant Biol.*, 2015, **66**, 23–48.
- 3 Y. Tachibana, L. Vayssieres and J. R. Durrant, *Nat. Photonics*, 2012, **6**, 511–518.
- 4 J. J. Concepcion, R. L. House, J. M. Papanikolas and T. J. Meyer, *Proc. Natl. Acad. Sci. U. S. A.*, 2012, **109**, 15560–15564.
- 5 G. Chen, G. I. N. Waterhouse, R. Shi, J. Zhao, Z. Li, L. Z. Wu, C. H. Tung and T. Zhang, *Angew. Chem., Int. Ed.*, 2019, **58**, 17528–17551.
- 6 K. Li, B. Peng and T. Peng, *ACS Catal.*, 2016, **6**, 7485–7527.
- 7 S. Chu, Y. Cui and N. Liu, *Nat. Mater.*, 2016, **16**, 16–22.
- 8 N. S. Lewis, *Science*, 2016, **351**, aad1920.
- 9 Q. Schiermeier, J. Tollefson, T. Scully, A. Witze and O. Morton, *Nature*, 2008, **454**, 816–823.
- 10 P. Nejat, F. Jomehzadeh, M. M. Taheri, M. Gohari and M. Z. A. Majid, *Renewable Sustainable Energy Rev.*, 2015, **43**, 843–862.
- 11 J. G. Canadell, C. Le Quéré, M. R. Raupach, C. B. Field, E. T. Buitenhuis, P. Ciais, T. J. Conway, N. P. Gillett, R. A. Houghton and G. Marland, *Proc. Natl. Acad. Sci. U. S. A.*, 2007, **104**, 18866–18870.
- 12 A. Fujishima and K. Honda, *Nature*, 1972, **238**, 37–38.
- 13 L. Cheng, Q. Xiang, Y. Liao and H. Zhang, *Energy Environ. Sci.*, 2018, **11**, 1362–1391.
- 14 J. Wen, J. Xie, X. Chen and X. Li, *Appl. Surf. Sci.*, 2017, **391**, 72–123.
- 15 Y. Zhang, D. Ma, J. Li, C. Zhi, Y. Zhang, L. Liang, S. Mao and J.-W. Shi, *Coord. Chem. Rev.*, 2024, **517**, 215995.
- 16 G. Jia, Y. Wang, X. Cui, H. Zhang, J. Zhao, L. H. Li, L. Gu, Q. Zhang, L. Zheng, J. Wu, Q. Wu, D. J. Singh, W. Li, L. Zhang and W. Zheng, *Matter*, 2022, **5**, 206–218.
- 17 H. Wang, L. Zhang, Z. Chen, J. Hu, S. Li, Z. Wang, J. Liu and X. Wang, *Chem. Soc. Rev.*, 2014, **43**, 5234–5244.
- 18 W. J. Ong, L. L. Tan, Y. H. Ng, S. T. Yong and S. P. Chai, *Chem. Rev.*, 2016, **116**, 7159–7329.
- 19 L. Jie, X. Gao, X. Cao, S. Wu, X. Long, Q. Ma and J. Su, *Mater. Sci. Semicond. Process.*, 2024, **176**, 108288.
- 20 M. Chen, J. Xiong, X. Li, Q. Shi, T. Li, Y. Feng and B. Zhang, *Sci. China: Chem.*, 2023, **66**, 2363–2370.
- 21 A. P. Côté, A. I. Benin, N. W. Ockwig, M. O'Keeffe, A. J. Matzger and O. M. Yaghi, *Science*, 2005, **310**, 1166–1170.
- 22 T. Banerjee, K. Gottschling, G. Savasci, C. Ochsenfeld and B. V. Lotsch, *ACS Energy Lett.*, 2018, **3**, 400–409.
- 23 L. Wang, L. Zhang, B. Lin, Y. Zheng, J. Chen, Y. Zheng, B. Gao, J. Long and Y. Chen, *Small*, 2021, **17**, e2101017.
- 24 Z. Liu, T. Ma, J. Liang, D. Si, T. Liu, F. Zhang, J. Sheng, Q. Wu and R. Wang, *Sci. China: Chem.*, 2025, **68**, DOI: [10.1007/s11426-024-2620-4](https://doi.org/10.1007/s11426-024-2620-4).
- 25 S. Thomas, H. Li, C. Zhong, M. Matsumoto, W. R. Dichtel and J.-L. Bredas, *Chem. Mater.*, 2019, **31**, 3051–3065.
- 26 J. Liu, G. Han, D. Zhao, K. Lu, J. Gao and T.-S. Chung, *Sci. Adv.*, 2020, **6**, eabb1110.
- 27 Q. Yang, M. Luo, K. Liu, H. Cao and H. Yan, *Appl. Catal., B*, 2020, **276**, 119174.
- 28 X. Li, K. Kawai, M. Fujitsuka and Y. Osakada, *Surf. Interfaces*, 2021, **25**, 101249.
- 29 N. Romero, R. Bofill, L. Francàs, J. García-Antón and X. Sala, *Catalysts*, 2021, **11**, 754.
- 30 J. You, Y. Zhao, L. Wang and W. Bao, *J. Cleaner Prod.*, 2021, **291**, 125822.



- 31 L.-J. Wang, P.-Y. Dong, G. Zhang and F.-M. Zhang, *Energy Fuels*, 2023, **37**, 6323–6347.
- 32 X. Han, J. Zhang, J. Huang, X. Wu, D. Yuan, Y. Liu and Y. Cui, *Nat. Commun.*, 2018, **9**, 1294.
- 33 S. Kandambeth, A. Mallick, B. Lukose, M. V. Mane, T. Heine and R. Banerjee, *J. Am. Chem. Soc.*, 2012, **134**, 19524–19527.
- 34 F. Haase and B. V. Lotsch, *Chem. Soc. Rev.*, 2020, **49**, 8469–8500.
- 35 Y. Peng, W. K. Wong, Z. Hu, Y. Cheng, D. Yuan, S. A. Khan and D. Zhao, *Chem. Mater.*, 2016, **28**, 5095–5101.
- 36 K. Dey, M. Pal, K. C. Rout, H. S. Kunjattu, A. Das, R. Mukherjee, U. K. Kharul and R. Banerjee, *J. Am. Chem. Soc.*, 2017, **139**, 13083–13091.
- 37 Y. Li, M. Zhang, X. Guo, R. Wen, X. Li, X. Li, S. Li and L. Ma, *Nanoscale Horiz.*, 2018, **3**, 205–212.
- 38 Y. Li, Q. Wu, X. Guo, M. Zhang, B. Chen, G. Wei, X. Li, X. Li, S. Li and L. Ma, *Nat. Commun.*, 2020, **11**, 599.
- 39 Y. Yang, S. Yao, Z. Liang, Y. Wen, Z. Liu, Y. Wu, J. Liu and M. Zhu, *ACS Energy Lett.*, 2022, **7**, 885–896.
- 40 H. S. Sasmal, A. Halder, H. S. Kunjattu, K. Dey, A. Nadol, T. G. Ajithkumar, P. Ravindra Bedadur and R. Banerjee, *J. Am. Chem. Soc.*, 2019, **141**, 20371–20379.
- 41 J. He, L. Yu, Z. Li, S. Ba, F. Lan and Y. Wu, *J. Colloid Interface Sci.*, 2023, **629**, 428–437.
- 42 H. Ma, B. Liu, B. Li, L. Zhang, Y. G. Li, H. Q. Tan, H. Y. Zang and G. Zhu, *J. Am. Chem. Soc.*, 2016, **138**, 5897–5903.
- 43 L. Zhang, X. Lu, J. Sun, C. Wang and P. Dong, *J. Mater. Chem. A*, 2024, **12**, 5392–5405.
- 44 Y. Xiao, K. Wang, W. Dong and L. Li, *Polymer*, 2024, **300**, 126980.
- 45 L. Yin, Y. Zhao, Y. Xing, H. Tan, Z. Lang, W. Ho, Y. Wang and Y. Li, *Chem. Eng. J.*, 2021, **419**, 129984.
- 46 R. Zhang, Z. D. Yang, Y. Yang, F. M. Zhang and G. Zhang, *ACS Appl. Mater. Interfaces*, 2023, **15**, 57265–57272.
- 47 X. Wang, L. Chen, S. Y. Chong, M. A. Little, Y. Wu, W. H. Zhu, R. Clowes, Y. Yan, M. A. Zwijnenburg, R. S. Sprick and A. I. Cooper, *Nat. Chem.*, 2018, **10**, 1180–1189.
- 48 Z. Lin, X. Yu, Z. Zhao, N. Ding, C. Wang, K. Hu, Y. Zhu and J. Guo, *Nat. Commun.*, 2025, **16**, 1940.
- 49 H. Wang, H. Wang, Z. Wang, L. Tang, G. Zeng, P. Xu, M. Chen, T. Xiong, C. Zhou, X. Li, D. Huang, Y. Zhu, Z. Wang and J. Tang, *Chem. Soc. Rev.*, 2020, **49**, 4135–4165.
- 50 X. Zhang, Z. Xiao, L. Jiao, H. Wu, Y. X. Tan, J. Lin, D. Yuan and Y. Wang, *Angew. Chem., Int. Ed.*, 2024, **63**, e202408697.
- 51 Z. Zhao, W. Chen, G. Zhang and Y. Chen, *J. Mater. Chem. A*, 2023, **11**, 26052–26062.
- 52 L. Hao, R. Shen, G. Liang, M. Kang, C. Huang, P. Zhang and X. Li, *Appl. Catal., B*, 2024, **348**, 123837.

